Editors' Suggestion | Featured in Physics

Bragg Coherent Modulation Imaging of Highly Strained Nanocrystals

Jiangtao Zhao*
ESRF, The European Synchrotron, 71 Avenue des Martyrs, 38000 Grenoble, France

Ewen Bellec and Marie-Ingrid Richard
ESRF, The European Synchrotron, 71 Avenue des Martyrs, 38000 Grenoble, France
and CEA, IRIG-MEM, Nanostructures and Synchrotron Radiation Laboratory, 38000 Grenoble, France

Linus Pithan and Ivan A. Vartanyants
Deutsches Elektronen-Synchrotron, Notkestraße 85, 22607 Hamburg, Germany

Fucai Zhang
State Key Laboratory of Quantum Functional Materials, Department of Electronic and Electrical Engineering, Southern University of Science and Technology, 518055 Shenzhen, China

Tobias Schülli† and Steven J. Leake‡
ESRF, The European Synchrotron, 71 Avenue des Martyrs, 38000 Grenoble, France

(Received 5 March 2025; revised 6 October 2025; accepted 27 October 2025; published 18 December 2025)

Bragg coherent diffraction imaging struggles to phase data from nanocrystals exhibiting large strain inhomogeneities, which significantly limits its applicability across many scientific scenarios. Here, we demonstrate the experimental realization of Bragg coherent modulation imaging, an approach that incorporates wavefront modulation into the diffracted beam, enabling unambiguous structure recovery and resolving highly strained crystals. This method provides a more robust tool for three-dimensional lattice strain measurements in nanocrystals.

DOI: 10.1103/8vrs-hjqm

Introduction—Bragg coherent diffraction imaging (BCDI) [1–3] exploits x-ray coherence [4] and phase retrieval [5–7] to measure three-dimensional (3D) lattice strain in crystals with a spatial resolution below 10 nm and a strain sensitivity down to 10^{-4} [8]. The 3D reciprocal space volume in the vicinity of a Bragg peak is measured; an intensity measurement leads to a classic phase problem where the amplitude is known and the missing phase information must be recovered using algorithms. The result is a 3D complex image (object function), where the modulus represents the Bragg crystallographic electron density and the phase corresponds to the projected lattice displacement along the Bragg reflection [9,10]. A natural extension involves measuring multiple noncoplanar Bragg reflections to obtain the full strain tensor for each voxel in an image [8,11,12]. BCDI has been applied to unveil the lattice strain effects in a variety of materials, including catalysts [13–15], ferroelectrics [16–18], semiconductors [19,20], and lithium battery materials [21–23], among others.

To date, BCDI applications have focused mainly on nanocrystals with relatively small deformation fields, where the reconstructed object phase values are restricted within the range of $[-\pi, \pi]$, equivalent to a unit cell of total deviation across the whole crystal [24,25]. However, in cases where multiple phase wraps are present, existing phase retrieval methods are relatively unsuccessful [26]. This is due to the inability to reliably resolve the shape function, the 3D volume of the crystal also known as the support constraint, and manifests as some nonphysical crystallographic electron density "gaps" in the reconstructed volumes [24]. Inherent to inverse problems is the coexistence of multiple equivalent solutions (twins) [27], which could be responsible for the difficulty in searching for the correct support function.

One way to overcome the aforementioned BCDI limitations is to add a wavefront modulator to the diffracted beam, a method coined Bragg coherent modulation imaging (BCMI) [28]. This provides a definitive constraint, if the modulator is well known, and allows for the unambiguous reconstruction of the diffracted signal. Numerical

*Contact author: jiangtao.zhao@esrf.fr
†Contact author: tobias.schulli@esrf.fr
‡Contact author: steven.leake@esrf.fr

simulations [28] show that BCMI demonstrates superior performance for highly strained nanocrystals and solves the twin problem of BCDI. The technique requires the insertion of a wavefront modulator after the sample, i.e., in the diffracted beam, which resolves its propagation ambiguities. The interference between the sample exit wave and a known modulator introduces a strong constraint in reciprocal space, which facilitates data inversion [29–31].

The experimental realization of BCMI, however, is not trivial. First, the wavefront modulator must be precisely positioned only a few millimeters downstream of the sample. Second, the modulator's transmission function must be accurately calibrated to provide essential *prior* knowledge required for the BCMI phase retrieval. Third, the modulator's high sensitivity to sample drift poses a significant challenge to effective data inversion [28]. Here, we present the first BCMI experimental demonstration at the ID01 beamline of the European Synchrotron Radiation Facility-Extremely Brilliant Source (ESRF-EBS, Grenoble, France) [32]. Viable solutions for modulator installation and calibration are suggested, along with the incorporation of a position correction algorithm into the BCMI phase retrieval process to address sample drift. Case studies of BCMI on low-strain (*LS*) and high-strain (*HS*) platinum (Pt) nanocrystals are presented, highlighting the superior reconstruction capabilities in terms of both accuracy and robustness compared with the current BCDI method.

Experiment—The experiment setup is shown in Fig. 1(a); it is similar to BCDI except that a wavefront modulator is inserted downstream, within a few millimeters, of the sample (d_1). The large sample-to-detector distance $d_1 + d_2 = 5.35$ m necessitates a horizontal scattering geometry, with the sample mounted vertically. The long detector arm is crucial for BCMI as it ensures the sufficient oversampling required for the ptychographic calibration of the modulator [30] in the diffracted beam where the beam is relatively large (several microns).

The modulator used in the experiment was made of a 1.5 μm thick layer of sputtered tungsten (W) deposited on a Si_3N_4 membrane and has a random structure fabricated by lithography. The random pattern has been optimized to have approximately 50% sparsity, and structural disconnectivity was avoided through a morphological filtering process [30]. The modulator was mounted on a specialized nanogoniometer, which was installed on the *eta* circle of the ID01 Huber diffractometer [see Fig. 1(b)]. The nanogoniometer (Supplemental Material S1 at [34]) offers three-axis translations (x, y, and z axes) and two-axis rotations (*Mchi* and *Mphi* axes), ensuring precise alignment of the modulator perpendicular to the Bragg diffracted beam direction. At an experimental x-ray energy of 9 keV, the theoretical induced phase shift ($\Delta\phi$) of this modulator on the incoming wavefront is calculated to be 2.4 rad, matching the modulator ptychographic calibration [see End Matter (EM) Appendix A] with the results shown in Fig. 1(c).

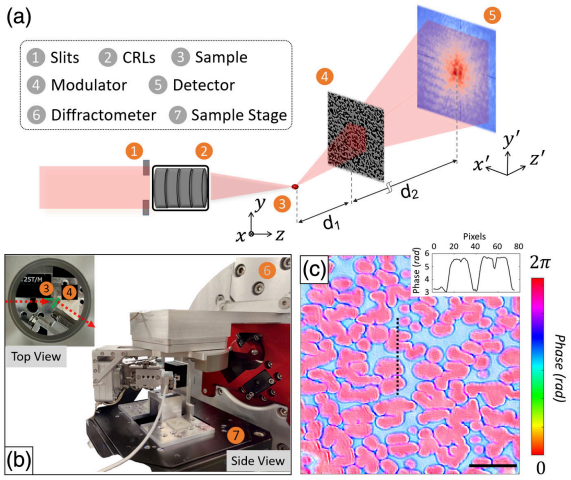

FIG. 1. BCMI experiment setup. (a) BCMI experiment schematic; CRLs, compound refractive lenses. The coordinates in the sample frame follows the CXI convention [33], i.e., x outboard, y vertical up, and z downstream. The coordinates in the detector frame are denoted as $x'y'z'$. (b) Photograph of the sample-modulator configurations. The modulator is mounted on the nanogoniometer (three translation axes on two rotation axes). The sample and modulator are highlighted with green outlines in top view, with the x-ray path indicated by a dashed red line. (c) Ptychographic reconstructed modulator function, with the modulus shown by brightness and the phase shown by color. Inset: the phase line plot at the location of the black dashed line. Scale bar is 1 μm.

We used dewetted Pt crystals with a size ranging from 100 to 800 nm as a model sample (Supplemental Material S2 at [34]). The crystals were predominantly oriented with the [111] direction perpendicular to the surface of the yttria-stabilized zirconium substrate. When the sample was mounted vertically, the (111) specular Bragg reflection was observed in the horizontal plane. The monochromatic incident beam was focused down to 1.5 μm using Beryllium compound refractive lenses (CRLs), with the coherent illumination defining slits set to 140 μm (x) × 300 μm (y) . Upon illumination of the target Pt nanocrystal, the diffracted beam scatters from the modulator and then propagates to the Eiger-2M detector [35]. The distance (d_1) for the measured *LS* and *HS* Pt is 1.35 ± 0.01 mm and 3.15 ± 0.01 mm, respectively, and these values were retrieved together with the ptychographic reconstruction of the modulator (Supplemental Material S3 at [34]).

The BCMI measurements were conducted immediately after the modulator calibration, rocking the Pt crystal within a range of $[-0.5°, 0.5°]$ at a step size of 0.005° around the (111) Bragg reflection. The exposure time for each diffraction slice was 1 sec. BCMI measurements were executed on two Pt nanocrystals: the *LS* Pt measuring $520 \times 740 \times 850$ nm^3, characterized by strain predominantly confined within the range of $[-0.05\%, 0.05\%]$,

and the *HS* Pt measuring $260 \times 810 \times 580$ nm^3, exhibiting a broader strain distribution spanning $[-0.2\%, 0.2\%]$ (see Supplemental Material S4 at [34] for data processing, which includes Refs. [17,36–38]). BCDI measurements were also performed using the same acquisition parameters for direct comparison by removing the modulator. Both the BCMI and BCDI diffraction data [39] were preprocessed for use, with the detailed information shown in Supplemental Material S4 at [34]. We note that, although the acquired BCMI data show approximately a 10% reduction in intensity compared to BCDI, this has a negligible impact on phase retrieval.

Results—As only the *LS* Pt crystal can be phased by BCDI, a direct comparison of BCDI and BCMI can be made. The reconstruction strategies are provided in EM Appendix B and Supplemental Material S5 and S6 at [34]. Figure 2 illustrates the BCMI and BCDI reconstruction properties and results. The BCMI reconstruction demonstrates strong robustness; all 100 reconstructions were successful and have a low error metric with free log-likelihood (LLK) [40] values around 6.0. The unique solution is also guaranteed [Fig. 2(b)]. By contrast, the BCDI reconstructions are highly sensitive to the initial object guess, as shown by the discrete distribution of the free-LLK values and multiple outcomes. These outcomes can be categorized into three types: correct (33%), conjugated (42%), and incorrect (25%) (see Supplemental Material S7 at [34]).

Figures 2(c) and 2(d) display the BCMI and BCDI reconstructed object functions, respectively. These were obtained by performing an eigen decomposition on the three best reconstructions (ranked by free-LLK index) and taking the first eigensolution, a common way to refine object estimates [40]. The relative weight of the first eigensolution for BCMI and BCDI reconstructions are 99.49% and 98.34%, respectively. Here BCMI demonstrates a superior reconstruction primarily due to its better modulus homogeneity, seen by a central peak of 0.64 in its normalized modulus histogram [Fig. 2(e)]. This aligns with expectations for such data inversion because the value of the shape function (modulus) ideally should be a constant [9]. The BCDI reconstruction, however, exhibits some inhomogeneity, and its modulus histogram displays a broader distribution with double peaks at 0.58 and 0.77. This modulus inhomogeneity can likely be attributed to the phase retrieval getting trapped in local minima. The resolution of the BCMI and BCDI reconstructions, evaluated using Fourier shell correlation (FSC) [41] with a 1/2-bit threshold (Supplemental Material S8 at [34]), was determined to be 24.4 and 45.8 nm, respectively, indicating that BCMI achieves a higher resolution [Fig. 2(f)].

The BCMI and BCDI reconstructions for the *HS* Pt nanocrystal employed the same strategy used for *LS* Pt. As anticipated, the BCMI *HS* Pt consistently maintains its superiority, demonstrating remarkable robustness and high

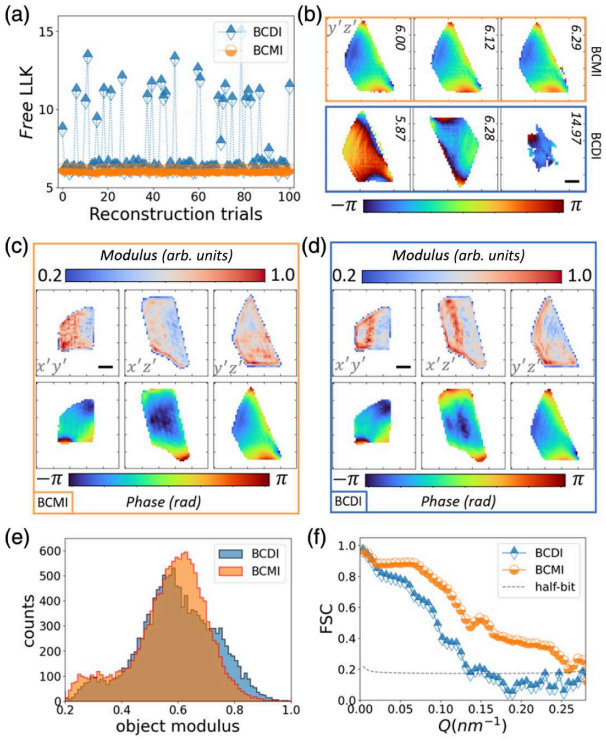

FIG. 2. BCMI and BCDI reconstruction results of *LS* Pt nanocrystal. (a) Free log-likelihood (LLK) plots of both BCMI and BCDI reconstruction trials. (b) Selected BCMI (upper row) and BCDI (bottom row) reconstruction results; only the $y'z'$ phase cross sections are shown, and the free-LLK values are marked on the panels. (c),(d) Central cross sections of BCMI and BCDI reconstructed objects; the phase offset has been removed for better comparison. (e) Histogram of the BCMI and BCDI reconstructed object modulus. (f) FSC plots of the BCMI and BCDI reconstructed objects. Images shown in (b)–(d) are in the detector conjugated space. Scale bar is 200 nm.

accuracy. All of these BCMI reconstructions yield similar results and exhibit small free-LLK values of approximately 2.13 [Figs. 3(a) and 3(b)]. The retrieved *HS* Pt object shows specific wrapped phase (highly strained) and still demonstrates modulus homogeneity, as shown in Figs. 3(c) and 3(e). We emphasize that the BCMI reconstruction properties for *HS* Pt surpass the capabilities of BCDI. This is identified by the high free-LLK values of BCDI reconstruction, ranging from [3.0, 4.3], and the incomplete retrieved results [Figs. 3(a) and 3(b)]. The BCDI reconstructions with other phase retrieval algorithms [6] are unlikely to provide significant improvement (see Supplemental Material Fig. S10 at [34]).

The primary challenge in BCDI phasing for highly strained crystals lies in the difficulty in finding the right support function using the shrink-wrap method [28,42]; the support is allowed to expand and contract between iterations. This often results in a completely erroneous update of the support, leading to a failed reconstruction. As a validation test, another set of BCDI reconstructions using a

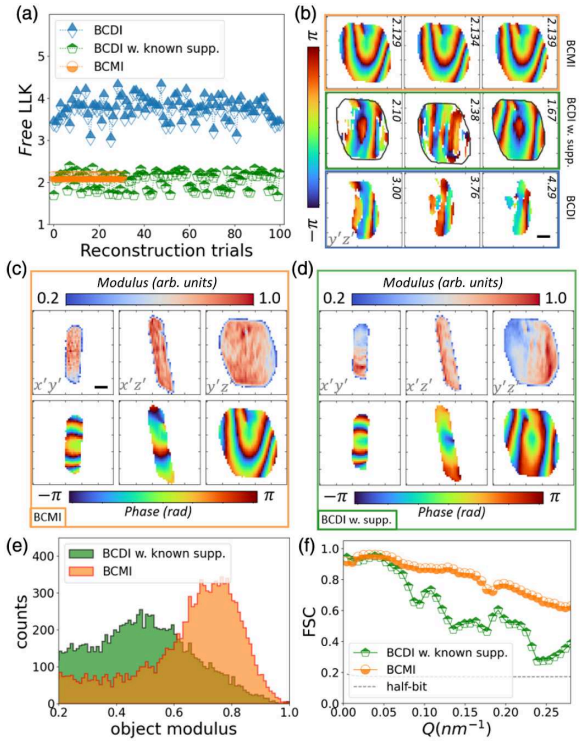

FIG. 3. BCMI and BCDI reconstruction results of *HS* Pt nanocrystal. (a) Free-LLK plots of the BCMI, known-support BCDI, and BCDI reconstruction trials. Because of the time-consuming nature, only 30 BCMI reconstruction trials were performed. (b) Selected BCMI (upper row), known-support BCDI (middle row), and BCDI (bottom row) reconstruction results; only the $y'z'$ phase cross section are shown, and the free-LLK values are marked on the panels. The black outline is used to guide the identification of conjugated solution. (c),(d) Central cross sections of BCMI and known-support BCDI reconstructed objects. (e) Histogram of the BCMI and known-support BCDI reconstructed object modulus. (f) FSC plots of the BCMI and known-support BCDI reconstructed objects. Images shown in (b)–(d) are in the detector conjugated space. Scale bar is 200 nm.

fixed known support function derived from the BCMI result was conducted. The BCDI approach, in this case, appears feasible but exhibits less robustness and lower accuracy compared to BCMI, as well as the lower spatial resolution. Despite having a low free-LLK value falling within the range of [1.7, 2.5], only 33% of reconstructions were successful. The lower success rate could be attributed to the symmetric shape of *HS* Pt and the competition of correct and conjugated solutions, as illustrated in Fig. 3(b). The retrieved object, shown in Fig. 3(d), showcases a noticeable modulus inhomogeneity, featuring a much broader distribution in its modulus histogram [Fig. 3(e)]. The modulus structures are highly correlated to the wrapped phase, which provides insight into why the shrink-wrap algorithm [42] becomes ineffective during the *HS* Pt reconstruction. We note that the differences in the BCDI and BCMI reconstructed object phase patterns arise from a slight crystal misorientation during measurement (see Supplemental Material Fig. S4 at [34]), which has a negligible impact on the assessment of reconstruction properties. The poor reconstruction performance on *HS* Pt underlines the limitations of BCDI and highlights the need for additional constraints such as the modulator constraint in BCMI.

Discussion and conclusions—The BCMI method integrates wavefront modulation into the diffracted beam, greatly enhancing the robustness, spatial resolution, and accuracy of image (phase) retrieval. The robustness of the BCMI approach relies on the modulation effect, which depends on the phase strength of the modulator (modulation magnitude) and the sample-to-modulator distance (effective modulation area). Under effective modulation, the accuracy of BCMI strongly depends on the modulator calibration and the magnitude of the sample drift. With the long detector arm, high stability of the sample stage, and a refined sample alignment procedure at ESRF-EBS ID01, we achieve reliable ptychographic calibration of the modulator and reduced sample drift.

This method, from the hardware perspective, requires an essential element of a wavefront modulator and a dedicated goniometer for precise installation and alignment. The modulator only needs to consider the material at the working x-ray energy and does not demand a complex design, making it relatively fabrication-friendly compared to high-precision x-ray focusing optics like Fresnel zone plates. From a software perspective, BCMI reconstruction needs significant computing power because of the slice-by-slice propagation model (see EM Appendix B). The near-field wavefront propagation and the position correction algorithm consume the most processing time. However, this could be improved through algorithm optimization such as parallel computing. The time-consuming aspects of the experiment involve modulator alignment and calibration. Excluding alignment, the calibration process typically takes 5 to 20 min when using ptychography, depending on the calibration area and the overlap ratio of the ptychographic scans.

Although BCMI introduces new challenges in both experimentation and data analysis, it provides valuable opportunities for studying highly strained nanocrystals and other complex samples in 3D. The main limitation of BCMI is the restricted sample environment due to the close proximity of the modulator to the sample, which currently limits its compatibility with existing *in situ* setups.

In summary, we have successfully demonstrated the experimental realization of the 3D BCMI method on isolated nanocrystals, overcoming implementation challenges and achieving precise measurements of highly strained crystals. This method has shown superior robustness and accuracy in image (phase) retrieval compared to standard BCDI. The unambiguous structure recovery and the unique capability to phase highly strained nanocrystals

paves the way for studying samples beyond the current capabilities of BCDI, enabling detailed insights into structural features like strain and defects. We anticipate that this new approach will become a routine tool for 3D strain characterization in nanomaterials.

Acknowledgments—We acknowledge the European Synchrotron Radiation Facility-Extremely Brilliant Source (ESRF-EBS) for provision of x-ray beam time under Proposal No. IHMI-1534. M.-I. R. acknowledges funding from the European Research Council (ERC) under the European Union's Horizon 2020 research and innovation program (Grant Agreement No. 818823). F. Z. acknowledges funding from the Shenzhen Science and Technology Innovation Program (No. JCYJ20241202125334045). We thank Professor Eugen Rabkin from Technion (Israel) for providing the samples.

J. Z., L. P., T. S., and S. L. implemented and optimized the experimental setup. J. Z., E. B., M.-I. R., L. P., T. S., and S. L. performed the experiment. J. Z. and E. B. analyzed the data using code developed by J. Z. and F. Z.. J. Z. wrote the manuscript. All authors interpreted the results and contributed to finalizing the manuscript.

Data availability—The data that support the findings of this article are openly available [39].

[1] I. K. Robinson, I. A. Vartanyants, G. J. Williams, M. A. Pfeifer, and J. A. Pitney, Reconstruction of the shapes of gold nanocrystals using coherent x-ray diffraction, Phys. Rev. Lett. **87**, 195505 (2001).

[2] M. A. Pfeifer, G. J. Williams, I. A. Vartanyants, R. Harder, and I. K. Robinson, Three-dimensional mapping of a deformation field inside a nanocrystal, Nature (London) **442**, 63 (2006).

[3] I. Robinson and R. Harder, Coherent x-ray diffraction imaging of strain at the nanoscale, Nat. Mater. **8**, 291 (2009).

[4] R. Khubbutdinov, A. P. Menushenkov, and I. A. Vartanyants, Coherence properties of the high-energy fourth-generation x-ray synchrotron sources, J. Synchrotron Radiat. **26**, 1851 (2019).

[5] J. R. Fienup, Phase retrieval algorithms: A comparison, Appl. Opt. **21**, 2758 (1982).

[6] S. Marchesini, Invited article: A unified evaluation of iterative projection algorithms for phase retrieval, Rev. Sci. Instrum. **78**, 011301 (2007).

[7] V. Favre-Nicolin, G. Girard, S. Leake, J. Carnis, Y. Chushkin, J. Kieffer, P. Paleo, and M.-I. Richard, *PyNX*: High-performance computing toolkit for coherent x-ray imaging based on operators, J. Appl. Crystallogr. **53**, 1404 (2020).

[8] M. C. Newton, S. J. Leake, R. Harder, and I. K. Robinson, Three-dimensional imaging of strain in a single ZnO nanorod, Nat. Mater. **9**, 120 (2010).

[9] I. A. Vartanyants and I. K. Robinson, Partial coherence effects on the imaging of small crystals using coherent x-ray diffraction, J. Phys. Condens. Matter **13**, 10593 (2001).

[10] V. Favre-Nicolin, F. Mastropietro, J. Eymery, D. Camacho, Y. M. Niquet, B. M. Borg, M. E. Messing, L.-E. Wernersson, R. E. Algra, E. P. A. M. Bakkers, T. H. Metzger, R. Harder, and I. K. Robinson, Analysis of strain and stacking faults in single nanowires using Bragg coherent diffraction imaging, New J. Phys. **12**, 035013 (2010).

[11] A. H. Mokhtar, D. Serban, D. G. Porter, F. Lichtenberg, S. P. Collins, A. Bombardi, N. A. Spaldin, and M. C. Newton, Three-dimensional domain identification in a single hexagonal manganite nanocrystal, Nat. Commun. **15**, 3587 (2024).

[12] D. Yang, A. F. Suzana, L. Wu, S. S. Ha, S. Choi, H. M. Ngo, M. M. Nawaz, H. Kim, J. Liu, D. Treuherz, N. Zhang, Z. An, G. Nisbet, D. G. Porter, and I. K. Robinson, Low-temperature state in strontium titanate microcrystals using *in situ* multireflection Bragg coherent x-ray diffraction imaging, Phys. Rev. B **111**, 024107 (2025).

[13] M. Dupraz, N. Li, J. Carnis, L. Wu, S. Labat, C. Chatelier, R. Van De Poll, J. P. Hofmann, E. Almog, S. J. Leake, Y. Watier, S. Lazarev, F. Westermeier, M. Sprung, E. J. M. Hensen, O. Thomas, E. Rabkin, and M.-I. Richard, Imaging the facet surface strain state of supported multi-faceted Pt nanoparticles during reaction, Nat. Commun. **13**, 3003 (2022).

[14] C. Atlan, C. Chatelier, I. Martens, M. Dupraz, A. Viola, N. Li, L. Gao, S. J. Leake, T. U. Schülli, J. Eymery, F. Maillard, and M.-I. Richard, Imaging the strain evolution of a platinum nanoparticle under electrochemical control, Nat. Mater. **22**, 754 (2023).

[15] R. A. Vicente, I. T. Neckel, S. K. R. S. Sankaranarayanan, J. Solla-Gullon, and P. S. Fernández, Bragg coherent diffraction imaging for *In Situ* studies in electrocatalysis, ACS Nano **15**, 6129 (2021).

[16] D. Karpov, Z. Liu, T. D. S. Rolo, R. Harder, P. V. Balachandran, D. Xue, T. Lookman, and E. Fohtung, Three-dimensional imaging of vortex structure in a ferroelectric nanoparticle driven by an electric field, Nat. Commun. **8**, 280 (2017).

[17] J. Diao, L. Wu, A. F. Suzana, E. S. Bozin, E. M. Zatterin, S. J. Leake, R. J. Harder, W. Cha, M. Abeykoon, J. Fan, H. Jiang, and I. K. Robinson, Behavior of strain stripe networks in barium titanate nanocrystals on crossing its ferroelectric phase transition, Phys. Rev. Mater. **8**, 016002 (2024).

[18] M. A. Najeeb, D. Serban, D. G. Porter, F. Lichtenberg, S. P. Collins, A. Bombardi, N. A. Spaldin, and M. C. Newton, Three-dimensional imaging of topologically protected strings in a multiferroic nanocrystal, Commun. Mater. **6**, 14 (2025).

[19] M. O. Hill, P. Schmiedeke, C. Huang, S. Maddali, X. Hu, S. O. Hruszkewycz, J. J. Finley, G. Koblmüller, and L. J. Lauhon, 3D Bragg coherent diffraction imaging of extended nanowires: Defect formation in highly strained InGaAs quantum wells, ACS Nano **16**, 20281 (2022).

[20] F. Berenguer, G. Pettinari, M. Felici, N. Balakrishnan, J. N. Clark, S. Ravy, A. Patané, A. Polimeni, and G. Ciatto, Imaging shape and strain in nanoscale engineered

semiconductors for photonics by coherent x-ray diffraction, Commun. Mater. **1**, 19 (2020).

[21] A. K. C. Estandarte, J. Diao, A. V. Llewellyn, A. Jnawali, T. M. M. Heenan, S. R. Daemi, J. J. Bailey, S. Cipiccia, D. Batey, X. Shi, C. Rau, D. J. L. Brett, R. Jervis, I. K. Robinson, and P. R. Shearing, *Operando* Bragg coherent diffraction imaging of $LiNi_{0.8}Mn_{0.1}Co_{0.1}O_2$ primary particles within commercially printed NMC811 electrode sheets, ACS Nano **15**, 1321 (2021).

[22] T. Liu, J. Liu, L. Li, L. Yu, J. Diao, T. Zhou, S. Li, A. Dai, W. Zhao, S. Xu, Y. Ren, L. Wang, T. Wu, R. Qi, Y. Xiao, J. Zheng, W. Cha, R. Harder, I. Robinson, J. Wen, J. Lu, F. Pan, and K. Amine, Origin of structural degradation in Li-rich layered oxide cathode, Nature (London) **606**, 305 (2022).

[23] D. Serban, D. G. Porter, A. H. Mokhtar, M. Nellikkal, S. Uthayakumar, M. Zhang, S. P. Collins, A. Bombardi, P. Li, C. Rau, and M. C. Newton, Imaging in-operando $LiCoO_2$ nanocrystallites with Bragg coherent x-ray diffraction, Commun. Chem. **7**, 243 (2024).

[24] M. C. Newton, R. Harder, X. Huang, G. Xiong, and I. K. Robinson, Phase retrieval of diffraction from highly strained crystals, Phys. Rev. B **82**, 165436 (2010).

[25] X. Huang, R. Harder, G. Xiong, X. Shi, and I. Robinson, Propagation uniqueness in three-dimensional coherent diffractive imaging, Phys. Rev. B **83**, 224109 (2011).

[26] A. A. Minkevich, E. Fohtung, T. Slobodskyy, M. Riotte, D. Grigoriev, M. Schmidbauer, A. C. Irvine, V. Novák, V. Holý, and T. Baumbach, Selective coherent x-ray diffractive imaging of displacement fields in $(Ga, Mn)As/GaAs$ periodic wires, Phys. Rev. B **84**, 054113 (2011).

[27] M. Guizar-Sicairos and J. R. Fienup, Understanding the twin-image problem in phase retrieval, J. Opt. Soc. Am. A **29**, 2367 (2012).

[28] J. Zhao, I. A. Vartanyants, and F. Zhang, Bragg coherent modulation imaging for highly strained nanocrystals: A numerical study, J. Appl. Crystallogr. **56**, 1528 (2023).

[29] F. Zhang and J. M. Rodenburg, Phase retrieval based on wave-front relay and modulation, Phys. Rev. B **82**, 121104 (2010).

[30] F. Zhang, B. Chen, G. R. Morrison, J. Vila-Comamala, M. Guizar-Sicairos, and I. K. Robinson, Phase retrieval by coherent modulation imaging, Nat. Commun. **7**, 13367 (2016).

[31] J. Soltau, M. Osterhoff, and T. Salditt, Coherent diffractive imaging with diffractive optics, Phys. Rev. Lett. **128**, 223901 (2022).

[32] S. J. Leake, G. A. Chahine, H. Djazouli, T. Zhou, C. Richter, J. Hilhorst, L. Petit, M.-I. Richard, C. Morawe, R. Barrett, L. Zhang, R. A. Homs-Regojo, V. Favre-Nicolin, P. Boesecke, and T. U. Schülli, The nanodiffraction beamline ID01/ESRF: A microscope for imaging strain and structure, J. Synchrotron Radiat. **26**, 571 (2019).

[33] CXIDB—coherent x-ray imaging data bank, available at, https://cxidb.org/cxi.html.

[34] See Supplemental Material at http://link.aps.org/supplemental/10.1103/8vrs-hjqm for materials and methods.

[35] I. Johnson, A. Bergamaschi, H. Billich, S. Cartier, R. Dinapoli, D. Greiffenberg, M. Guizar-Sicairos, B. Henrich, J. Jungmann, D. Mezza, A. Mozzanica, B. Schmitt, X. Shi, and G. Tinti, Eiger: A single-photon counting x-ray detector, J. Instrum. **9**, C05032 (2014).

[36] D. Simonne, J. Carnis, C. Atlan, C. Chatelier, V. Favre-Nicolin, M. Dupraz, S. J. Leake, E. Zatterin, A. Resta, A. Coati, and M.-I. Richard, *Gwaihir: Jupyter Notebook* graphical user interface for Bragg coherent diffraction imaging, J. Appl. Crystallogr. **55**, 1045 (2022).

[37] O. Gorobtsov and A. Singer, Shear displacement gradient in x-ray Bragg coherent diffractive imaging, J. Synchrotron Radiat. **29**, 866 (2022).

[38] F. Hofmann, N. W. Phillips, S. Das, P. Karamched, G. M. Hughes, J. O. Douglas, W. Cha, and W. Liu, Nanoscale imaging of the full strain tensor of specific dislocations extracted from a bulk sample, Phys. Rev. Mater. **4**, 013801 (2020).

[39] Data supporting the findings of this study are accessible via, 10.15151/ESRF-DC-2270287529.

[40] V. Favre-Nicolin, S. Leake, and Y. Chushkin, Free log-likelihood as an unbiased metric for coherent diffraction imaging, Sci. Rep. **10**, 2664 (2020).

[41] M. Van Heel and M. Schatz, Fourier shell correlation threshold criteria, J. Struct. Biol. **151**, 250 (2005).

[42] S. Marchesini, H. He, H. N. Chapman, S. P. Hau-Riege, A. Noy, M. R. Howells, U. Weierstall, and J. C. H. Spence, X-ray image reconstruction from a diffraction pattern alone, Phys. Rev. B **68**, 140101(R) (2003).

[43] A. M. Maiden and J. M. Rodenburg, An improved ptychographical phase retrieval algorithm for diffractive imaging, Ultramicroscopy **109**, 1256 (2009).

[44] A. G. Shabalin, M. Zhang, W. Yao, R. Rysov, Z. Ren, D. Lapkin, Y.-Y. Kim, D. Assalauova, N. Mukharamova, M. Sprung, I. A. Vartanyants, Y. S. Meng, and O. G. Shpyrko, Mapping the 3D position of battery cathode particles in Bragg coherent diffractive imaging, J. Synchrotron Radiat. **30**, 445 (2023).

[45] F. Zhang, I. Peterson, J. Vila-Comamala, A. Diaz, F. Berenguer, R. Bean, B. Chen, A. Menzel, I. K. Robinson, and J. M. Rodenburg, Translation position determination in ptychographic coherent diffraction imaging, Opt. Express **21**, 13592 (2013).

[46] W. Cha, A. Ulvestad, M. Allain, V. Chamard, R. Harder, S. J. Leake, J. Maser, P. H. Fuoss, and S. Hruszkewycz, Three dimensional variable-wavelength x-ray bragg coherent diffraction imaging, Phys. Rev. Lett. **117**, 225501 (2016).

[47] P. Li, S. Maddali, A. Pateras, I. Calvo-Almazan, S. Hruszkewycz, W. Cha, V. Chamard, and M. Allain, General approaches for shear-correcting coordinate transformations in Bragg coherent diffraction imaging. Part II, J. Appl. Crystallogr. **53**, 404 (2020).

[48] D. Yang, N. W. Phillips, and F. Hofmann, Mapping data between sample and detector conjugated spaces in Bragg coherent diffraction imaging, J. Synchrotron Radiat. **26**, 2055 (2019).

End Matter

Appendix A: Modulator calibration—We calibrated the modulator using ptychography [43] with the Bragg diffracted beam, specifically using the most intense Pt (111) diffracted beam as the illumination. The ptychographic scan was performed in the x-y plane perpendicular to the diffracted x-ray beam using the Smaract piezo motors of the nanogoniometer; a scan area of 6×6 μm^2 resulted using a spiral trajectory with a step size of 120 nm. In the current demonstration, the modulator calibration was performed each time when changing the measured crystal. Figure 1(c) and Fig. S2 (b) show the ptychographic reconstructed modulator functions for the *LS* and *HS* Pt nanocrystals, where the modulator's 2.45 rad phase shift matches the theoretical calculation value given by the formula $\Delta\phi = (2\pi/\lambda)\delta t$, where λ is the x-ray wavelength, δ is the real part of the refraction index of W at the current x-ray energy, and t is its thickness. The modulator reconstruction defines the achievable spatial resolution in the final BCMI reconstruction; as the data was cropped we expect to achieve a pixel-size resolution of 23 nm (see Supplemental Material S3 and Fig. S2 at [34]). The merits of using ptychography under the crystal diffraction beam to calibrate the modulator are summarized in Supplemental Material S3 at [34].

Appendix B: BCMI reconstruction—The BCMI reconstruction employed an optimized phase retrieval algorithm, with a key modification to correct for sample drift [44] introduced by integrating a position correction scheme [45]. This correction is essential because the modulator is highly sensitive to drift, with the position information being directly encoded in the diffraction patterns. Without accounting for this effect, artifacts and image distortions would arise. By contrast, this issue does not occur in BCDI as long as the beam is large enough, due to the Fourier shift theorem.

The optimized BCMI propagation model (forward and backward) is written as

$$\psi_j = \mathcal{F}_{m\to D}\mathcal{M}\mathcal{P}_{o\to m}\{\mathcal{T}\mathcal{R}\mathcal{Q}_j\rho\}$$

and

$$\rho = \sum_{j=1}^{J} \mathcal{Q}_j^{*}\mathcal{R}^{\dagger}\mathcal{T}^{-1}\mathcal{P}_{m\to o}^{-1}\mathcal{M}^{-1}\mathcal{F}_{D\to m}^{-1}\{\psi_j\},$$

with notation detailed in Supplemental Material Table S2 at [34]. It describes BCMI wavefront propagation in three steps at each rocking angle j, through the wavefront propagator $\mathcal{P}$, the modulation operator $\mathcal{M}$, and the Fourier transform $\mathcal{F}$. The operator $\{\cdot\}^{-1}$ is the inverse of the operator $\{\cdot\}$ (where $\cdot = \mathcal{P}$, $\mathcal{M}$, and $\mathcal{F}$), with the subscript o, m, and D indicating the computational plane of the object, modulator, and detector, respectively. The projection $\mathcal{R}$ and back-projection $\mathcal{R}^{\dagger}$ operator, along with the angle-associated phase terms $\mathcal{Q}_j$ and $\mathcal{Q}_j^{*}$ (the conjugate), facilitate the dimensional transformation of the object ρ between 3D and 2D, enabling the slice-by-slice calculation to be conducted effectively [28,46,47]. The translation operators $\mathcal{T}$ and $\mathcal{T}^{-1}$ were introduced to correct sample drift and are defined as $\mathcal{T}$: $f(x - s_x^j, y - s_y^j)$ and $\mathcal{T}^{-1}$: $f(x + s_x^j, y + s_y^j)$, where the sample shift values s_x^j, s_y^j would be retrieved by correlation calculation of phase-modulated object projections ρ_j ($\mathcal{R}\mathcal{Q}_j\rho$) and their updates ρ_j' (i.e., the projections after applying the modulus constraint). Implementation of BCMI phase retrieval is provided in Supplemental Material S5 at [34].

Another key point to reach a successful BCMI reconstruction is that the phase retrieval algorithm needs a support guess function (located in detector conjugated space [48]) with correct voxel positions, primarily in the x'-y' plane. Again, this is due to the position encoding effect of the modulator. To generate this support (see Supplemental Material Fig. S8 at [34]), we first need to search the reconstruction window and determine the pixel size in the x'-y' plane by phasing the central $x'y'$ BCMI diffraction data. Subsequently, we combine the pixel size range in the z' axis, evaluated from the autocorrelation function, to generate a cube-shaped support function. The BCMI reconstructed object will be confined in the support region.